Alma Mater Studiorum · University of Bologna

School of Science
Bachelor's degree in Physics

Λ_c detection using a weighted Bayesian PID approach

Supervisor:
Prof. Silvia Arcelli

Co-supervisor:
Dr. Francesco Noferini

Presented by:
Marco Giacalone

Session II
Academic Year 2015/2016

To my family

Contents

Introduction

The aim of this thesis is to evaluate the performance of the ALICE detector for the detection of the Λ_c baryon in PbPb collisions using a novel approach for particle identification (PID) .
The main idea in the new approach is the replacement of the usual cut–based selection on the detector signals with one that uses the probabilities derived from the Bayes theorem (used as weight), namely "Weighted Bayesian".
In order to provide a quantitative statement and to establish which method is the most efficient, a comparison with other standard PID approaches used in ALICE is presented. To do that a fast Monte Carlo simulation software, tuned on the particle abundances expected in the new LHC regime and on the observed detector performance was implemented.
Therefore, a realistic estimate of the Λ_c production in PbPb collisions was derived, combining the known results from previous experiments, and this was used to evaluate the significance after RUN2 and RUN3 data taking LHC periods.
This dissertation is composed by three chapters:
The physics studied by ALICE will be briefly described in the first chapter, touching topics like the standard model, quantum chromodynamics and the quark gluon plasma. Furthermore, a summary of the latest analysis results at RHIC and at LHC will be described. The second chapter contains a description of ALICE detector, reporting its structure and explaining how its principal components work. These are followed by a discussion on particle identification in ALICE and eventually by a description of the new bayesian approach tested in the simulations presented in this thesis. Finally, the last chapter describes how the simulation and the analysis were performed, and the results obtained with different PID approaches are presented.

Chapter 1

ALICE physics

1.1 A brief introduction to the Standard Model

The relation among fundamental particles and three of the four fundamental forces is nowadays described by the *Standard Model* (SM), which, starting from 12 elementary particles and 3 fundamental forces (electromagnetic, nuclear weak and nuclear strong), can explain all the complex processes in particle physics until now.

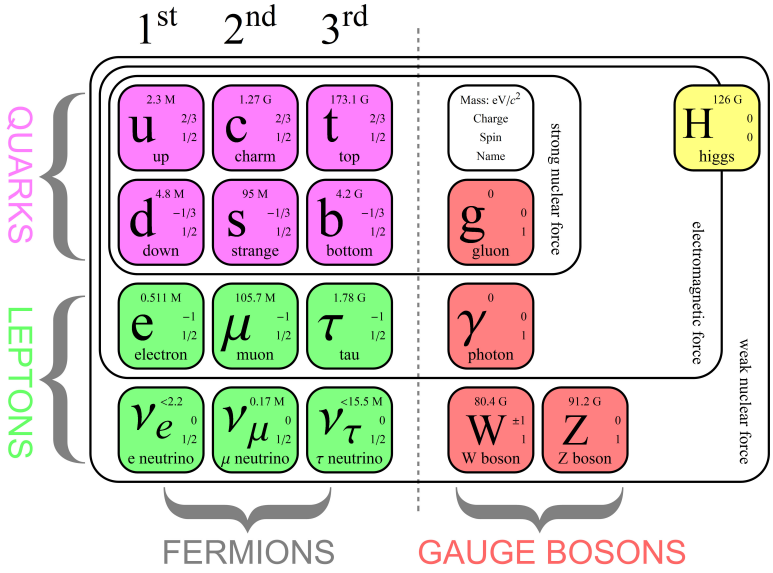

Figure 1.1: Standard Model.

As can be seen from Figure 1.1, the SM comprises 17 kinds of elementary particles: 12 particles of matter (all of them being fermions, with spin $= \frac{1}{2}$) and the corresponding antiparticles, 4 types of interaction carriers (all of them being bosons with spin $= 1$) and the Higgs boson (having spin $= 0$), which has the simple, but non-trivial, task to give mass to other particles through its interaction with them. The $W^{\pm}, Z$ bosons are the carriers of the weak nuclear interaction, photons (γ) are the electromagnetic interaction

carriers and gluons (g) carry the strong nuclear interaction.
The only fundamental force that the SM does not describe is the gravitational one, because using Quantum Field Theory (QFT), that is the language used to express the SM itself, it can be found that gravitational interaction is not renormalizable. Even though, theoretically, an elementary particle with spin = 2 that could mediate the gravitational force has been theorized (the graviton), it has not been experimentally discovered yet.
As can be seen in Fig. 1.1 there are three fermions generations (labeled 1^{st}, 2^{nd} and 3^{rd}) each containing particles with similar interaction properties.
Each of the three interactions described in the SM can be explained using gauge and group theories:

- the electromagnetic interaction derives from the *gauge* invariance of group $U(1)$;
- the weak nuclear interaction from $SU(2)_L$, where the L means only left-handed particles have weak charge[1][2];
- the strong nuclear interaction from $SU(3)$ of colour charges.

The last one yields to the quantum field theory of the strong interaction that is the basis of ALICE physics: the Quantum ChromoDynamics (QCD)[1] .

1.2 Quantum Chromodynamics (QCD)

ALICE is designed to study the physics of strongly interacting matter at extreme energy densities.
Quantum Chromodynamics is a quantum field theory describing interaction among quarks and gluons. To express the strength of the strong force the coupling constant α_s is used.
The Quantum ElectroDynamics (QED), which is the QFT of the electromagnetic interaction, has a coupling constant, also known as fine-structure constant, equal to:

$$\alpha_{em} = \frac{e^2}{4\pi\epsilon_0\hbar c} \simeq \frac{1}{137}.$$

It is possible to estimate the relative strength of the couplings α_s and α_{em} using mean lifetimes of two particles with similar masses decaying respectively according to the two interactions mentioned before. Particles decaying via the strong nuclear force have a mean life of approximately $10^{-23}s$, while those decaying via the electromagnetic interaction of about $10^{-19}s$, so the following relation holds:

$$\frac{\alpha_s}{\alpha_{em}} \simeq \left(\frac{10^{-19}}{10^{-23}}\right)^{\frac{1}{2}} \simeq 100\,.$$

[1] As discovered by Wu experiment and later explained by E.C.G. Sudarshan.
[2] The electromagnetic and weak interactions are then unified and described by the combination $SU(2)_L \times U(1)_Y$, where Y is the weak hypercharge.

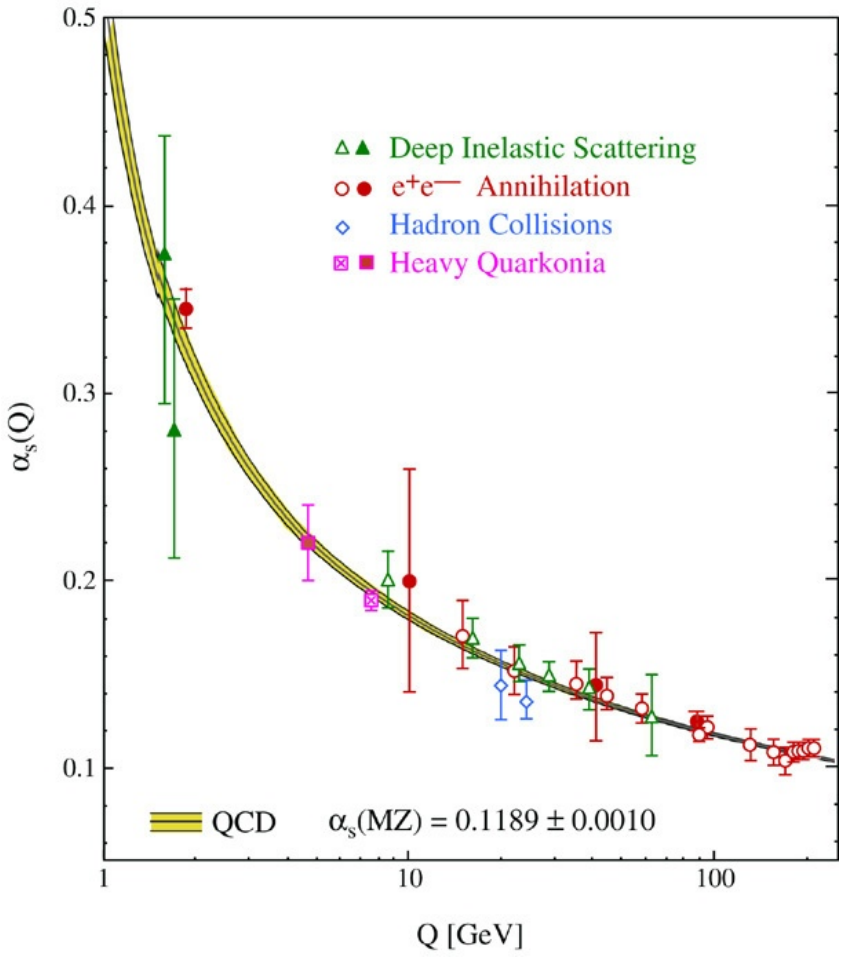

Figure 1.2: "Running" coupling constant $\alpha_s(Q)$ as a function of the exchanged momentum Q. The graph shows also a typical value which is the scale of the mass M_Z of the boson Z^0.

The coupling constant α_s, like α_{em}, depends on the momentum transfer Q, and at first order it is:

$$\alpha_s(Q) = \frac{12\pi}{(33 - 2N_f)\ln\dfrac{Q^2}{\Lambda^2}},$$

valid for $Q^2 >> \Lambda^2$, where N_f is the number of quark flavours and $\Lambda = 0.2 \pm 0.1$ GeV is an experimentally determined cutoff value.[2]
However, unlike electromagnetic fields, gluonic ones increase their strength with distance (almost linearly in some cases). This implies that the strong nuclear force is small in the proximity of a colour charge and increasingly stronger far from it and, for this reason, a colour charge can, in the former case, be considered almost free. This property is called *Asymptotic freedom*, theoretically explained by D. Gross, D. Politzer and F. Wilczek, who later (2004) won the Nobel Prize. [3]

The fact that the strong interaction gets "stronger" with distance bears to another property, that is the impossibility to separate quarks: this is *confinement*. In fact a non-bounded quark has never been observed and, even though until now there is no a proof that confinement can be derived from QCD[4, from p.129], it is a common belief that this property is the cause of this behaviour.
Unfortunately, while at high energy a perturbative approach can be applied, due to asymptotic freedom, this is not possible for low Q.

1.3 Quark-gluon plasma (QGP)

In low energy condition (less than 1 GeV) quarks are bounded and form the hadrons (with a typical radius of $\sim$ 1fm). But, as theoretically demonstrated, the coupling constant depends on temperature and baryonic density. In particular, it decreases for high temperature and/or high baryonic density. In this situation hadronic matter is no longer made by bounded quarks and gluons and it is not color-neutral, but quarks and gluons are free to move, forming a state called Quark-Gluon Plasma.

1.3.1 Phase Transition in QCD

At the boundary between these two obviously different matter states (hadronic matter and the QGP), a phase transition can be expected at a temperature T_c (critical temperature), which can be estimated to be $\sim$ 170 MeV.

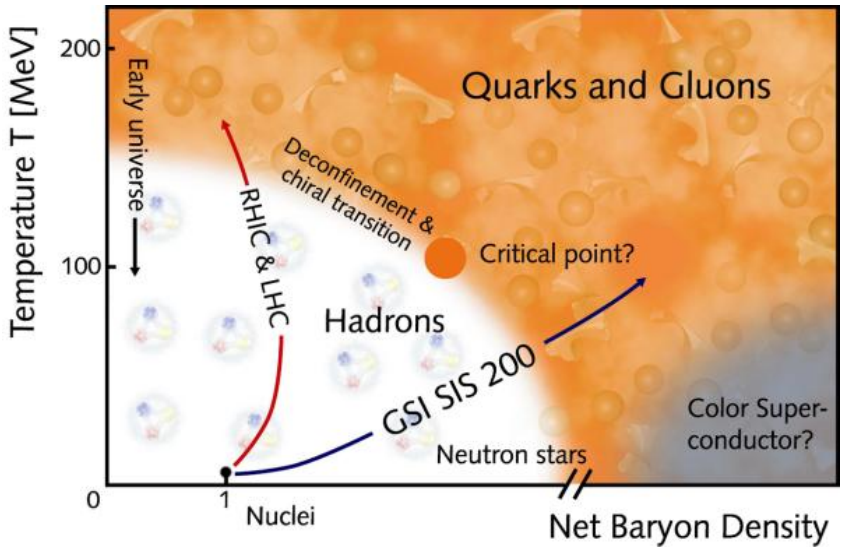

Figure 1.3: Phase diagram of QCD.

Another relevant parameter is the baryochemical potential μ_B, which is the needed en-

ergy to increase by one the quantum baryon number, i.e:

$$\mu_B = \frac{\partial E}{\partial N_B},$$

where N_B is the number of baryons. From μ_B the Net Baryon density (horizontal axis of Fig. 1.3) can be derived, i.e. the density of protons and neutrons[3] minus the density of antibaryons. It can be seen also that at the boundary between the hadronic and the QGP phase the growth of the baryochemical potential causes a decrease in the value of the critical temperature.[5]
Referring still to the Fig. 1.3, the diagram shows that having a low net baryon density ($\mu_B \to 0$) and low temperature leads to a confined hadron gas, but if the temperature is increased the gas will change its behaviour since quarks, gluons and antiquarks will split and will be free to move. This condition is called *deconfinement* because those particles move over distances larger than 1 fm[4].
This is how matter was supposed to be in the early Universe at a few μs after the Big Bang. In this case baryons and antibaryons are almost equal in number, for this reason $\mu_B \to 0$ and the order parameter of the phase transition, which is a measure of the degree of order across the boundaries in a phase transition system, is a crossover (it diverges). On the other hand, for larger μ_B and beyond the critical point, where the phase transition temperature decreases as a consequence of a gain in the density, the order parameter becomes 1 (like for water phase transition). This means that in the former case the transition is continuous (all derivatives of free energy are continuous at the transition), while in the latter case it shows a discontinuity that leads to a latent heat during the phase transition (discontinuity of first derivative on free energy[5]).

1.3.2 QGP Production

Extreme conditions of high density and temperature, needed to create the QGP, can be reached using nuclei collisions at extremely high energy.
Lattice QCD calculations predict that, as already seen, the critical temperature at which a transition from hadronic matter to QGP can occur is $T_C = (175 \pm 15)$MeV corresponding to a critical energy density $\epsilon_C \sim (0.3 \div 1.3)\text{GeV/fm}^3$. Moreover calculations show also how the phase transition is followed by a quick increase of the energy density ϵ and of the entropy s.
As for confinement, to investigate the phase transition from a theoretical point of view a perturbative approach can not be used, but it can be studied using a QCD lattice.
The quark-gluon plasma is not actually a real plasma, but it behaves more like a strongly interacting Fermi liquid (a theoretical model of interacting fermions), as experimentally observed.

[3] They are both baryons.
[4] Typical dimension of an hadron, as said before.
[5] The system receives energy, but the temperature does not increase in the transition state.

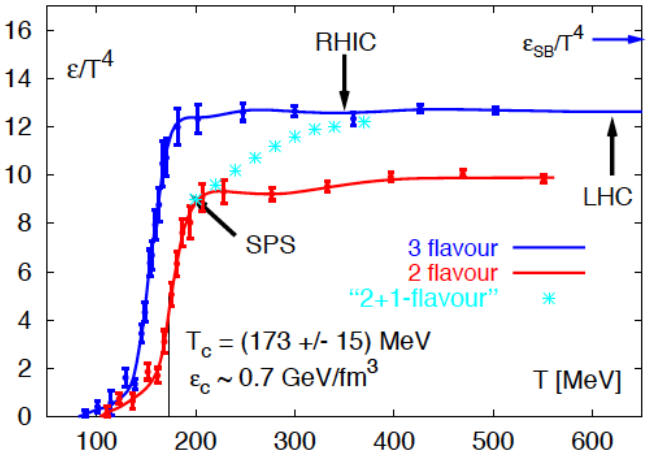

Figure 1.4: Energy density in units of T^4 as a function of temperature T. Points are obtained using lattice QCD simulations and the three curves refer to three hypothesis on the degrees of freedom associated to contributing flavours.

In colliders, such as the *Large Hadron Collider* (LHC) or the *Relativistic Heavy Ion collider* (RHIC), the nuclei in particle beams (Lead ones for the former and Gold ones for the latter) are accelerated to ultrarelativistic speed and directed towards each other, so that in the rare event of a collision, matter would be heated up to a temperature of at least $2 \cdot 10^{12}$K, creating a *fireball* in which everything is melted into a quark-gluon plasma.
While expanding under its own pressure, this fireball cools down during a process called *freeze-out* that can be divided in two stages: the chemical one and the kinematic one.
During the chemical freeze-out, after $\sim 10^{-23}$s from the nuclei collision, quarks and gluons in fluid state begin to generate hadrons which will fix particles abundancies and will yield to the final hadronic spectrum. So during this step an inverse phase transition happens (from QGP to regular hadronic matter)[6].
After mutual distances among these newborn particles exceed the typical distance range of the strong interaction, the inelastic processes of matter creation stop and the elastic *kinematic freeze-out* begins, when momentum spectra of particles can change due to elastic collisions or resonance decays, but ratios of the produced particles are fixed.[7]

1.3.3 Analysis of signals

Generally, to characterize particle production the following kinematic variables are used:

- *longitudinal momentum* p_L, that is the momentum projection on the direction of the particles beam propagation axis (z in this case);
- *transverse momentum* $p_{\mathrm{T}} = \sqrt{p_x^2 + p_y^2}$, where p_x and p_y are the other two compo-

nents of the momentum;

- *rapidity*, defined as:

$$Y = \frac{1}{2} \ln \left(\frac{E + p_L}{E - p_L} \right) = \tanh^{-1} \left(\frac{p_L}{E} \right),$$

where E is the particle energy and the reference frame is the center of mass;

- *pseudorapidity*, defined as:

$$\eta = \frac{1}{2} \ln \left(\frac{p + p_L}{p - p_L} \right) = - \ln \left(\tan \frac{\theta}{2} \right),$$

which is the approximation of the ultra-relativistic limit of rapidity, where E $\approx$ p, and θ is the angle between the particle momentum and the z axis. [8, p.8]

- *centrality*, defined by the nucleons number which take part in collisions ($N_{partecipants}$). It is a key parameter useful to study the properties of heavy ion collisions. The centrality percentile c of an A-A collision is:

$$c = \frac{\int_0^b \mathrm{d}\sigma/\mathrm{d}b \, \mathrm{d}b}{\int_0^\infty \mathrm{d}\sigma/\mathrm{d}b \, \mathrm{d}b} = \frac{1}{\sigma_{AA}} \int_0^b \frac{\mathrm{d}\sigma}{\mathrm{d}b} \, \mathrm{d}b \, .$$

where $\mathrm{d}\sigma/\mathrm{d}b$ is the impact parameter distribution (σ is the total nuclear interaction cross section and b is the impact parameter).[18]

The lifetime of deconfinement phase and, consequently, of the existence of QGP, is very short, so to investigate whether the fireball has actually formed or not is a complex task. Hence several signals which can lead to understand the evolution of the collisions are used.
In particular, a wide variety of experimental probes are used to study different aspects of the produced fireball.

Strangeness enhancement

The final stage of the phase transition leads to an enhancement in strangeness production as a consequence of the restoration of chiral symmetry, lost during the transition between hadronic gas and QGP [6].
As a matter of fact, the threshold for the production of an $s\bar{s}$ pair (forming a ϕ^0 meson) reduces by the double the mass of the constituent strange quark, which is $\sim$ 450 MeV, to twice the intrinsic mass of the quarks, that for the strange quark is $\sim$ 100 MeV.

[6] Chiral symmetry can be considered an approximate symmetry of QCD in the limit of vanishing quark masses[9].

So, given that the energy needed for the pair production is substantially reduced, a copious production of ϕ^0 is expected in the high density fireball during its cooling, mostly by gluon fusion ($g + g \rightarrow s + \bar{s}$). Furthermore, the deconfined phase can yield also to the enhanced production of baryons with multiple strange quarks, e.g. Ξ^0 (uss), Ξ^- (dss) and Ω^- (sss).[10]

J/ψ production

With the formation of a hot QGP, colour screening should prevent $c\bar{c}$ and $b\bar{b}$ binding in the deconfined stage.
These $c\bar{c}$ and $b\bar{b}$ states are called *quarkonia* (*charmonium* and *bottomonium*) and the effects from QGP can be seen through the suppression of J/ψ and Y states, whose only cause seems to be the creation of a deconfined plasma.
The basic mechanism for deconfinement in dense matter is the Debye screening of quark colour charge[7]. This implies that when the screening radius r_D becomes less than the binding radius r_H of the quark system, i.e. less than the hadron radius, the confining force can no longer hold the quarks together, and deconfinement sets in.
So, in the case of J/ψ production one expects that the hotter the medium the lower the observed yield would be, due to a reduction of the screening radius at temperatures higher than T_c, i.e. the deconfinement temperature ($\sim$ 170 MeV as above). Hence for T $\simeq T_c$ a small decrease should be observed while for T $\gg T_c$ J/ψ production should vanish. [11]
On the other hand other theoretical considerations suggest that J/ψ production in the QGP is a more complex mechanism. As a matter of fact there could be an enhancement given by quark recombination due to the large number of $c\bar{c}$ pairs produced in high energy collisions at LHC which could lead to an important source of charmonium. Even now there are uncertainties in the prevailing conditions at the initial stage of the collision [12].

Photons and dileptons spectra

One of the most sensitive probes of the QGP formed in ultra-relativistic collision of heavy ions are electomagnetic ones, i.e. photons and di-leptons (pairs of correlated leptons and antileptons). These particles do not carry colour charge, so they are minimally scattered inside the coloured medium. Moreover, they are emitted in different phases of the process. Since they are emitted over the entire history of the collision, from the nuclei scattering to the *freeze-out*, it is important to use proper models for the evolutions of heavy-ion collisions final states. Doing so the various sources contributing to the final observables could be disentangled and a more precise study of the QGP characteristics could be done[13].

[7]The Debye length is the distance within which, in this case, colour charge screens strong nuclear field.

The most interesting photons are the ones having little transverse momentum p_{T}, emitted by deconfined matter and called *thermal photons*.

1.4 Summary of RHIC and LHC results

The most recent data about heavy ions collisions are those obtained at the RHIC collider, located at Brookhaven National Laboratory (BNL) and built in 2000, and at the LHC, located at the European Organization for Nuclear Research laboratories (CERN) in Geneva[14].
The most energetic Au-Au collisions at RHIC had a $\sqrt{s_{NN}} = 200$ GeV, where $\sqrt{s_{NN}}$ is the energy of the nucleons pair colliding in the center of mass, while the most energetic Pb-Pb collisions at LHC, during the first LHC run, had a $\sqrt{s_{NN}} = 2.76$ TeV.
The initial temperature can be evaluated from the lattice QCD assuming $\mu_B \sim 0$, that gives an estimation of the initial temperature at RHIC of 240-320 MeV and of 310-370 MeV at LHC.
Combined efforts of different collaborations both from LHC and RHIC, e.g. PHOBOS, STAR, PHENIX at RHIC and ALICE, ATLAS and CMS at LHC, were required to achieve the following results.

1.4.1 Charged multiplicity

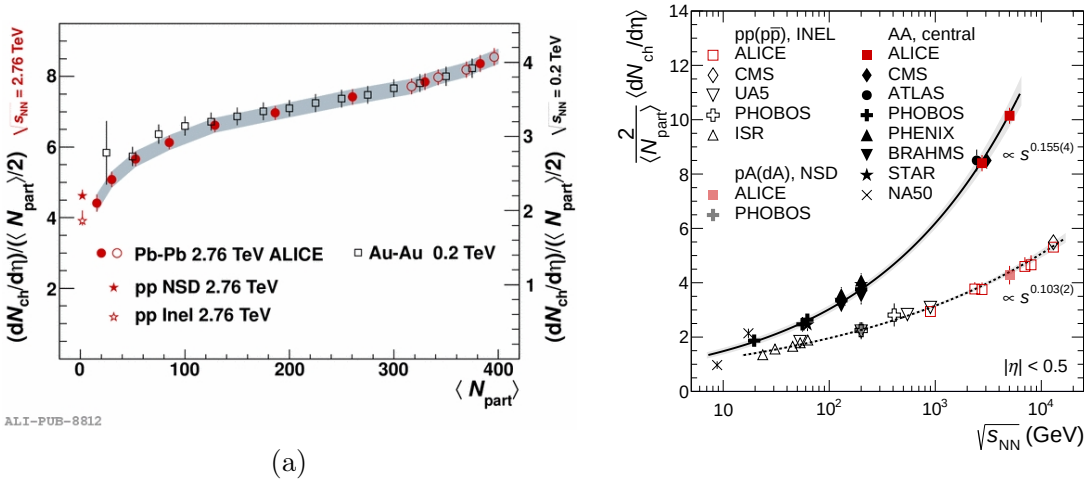

(a) (b)

Figure 1.5: Charged particles pseudo-rapidity density per participant pair for central nucleus-nucleus collisions as a function of nucleons participating in the collisions (a) and as a function of the collision energy (b).

The multiplicity[8] of charged particles $\frac{\mathrm{d}N_{ch}}{\mathrm{d}\eta}$ was measured both at RHIC and at LHC

[8]The total number of particles produced in a collision.

and results are shown in Fig. 1.5 .[15]
Considering the increase of the mean hadron transverse momentum at the LHC, the initial energy density for PbPb collisions is about three times larger than in AuAu collisions at RHIC, and they are both larger than the critical energy density to create deconfined matter.
The hadron yield ratios can be described using a thermal statistical model, whose theoretical predictions can be compared to those obtained from colliders.
The fit of experimental data are particularly useful to estimate the baryochemical potential and the chemical *freeze-out* temperature: as theoretically hypothesized the latter is ~ 160 MeV in both cases, which is indeed very close to the phase transition temperature as predicted by lattice calculations, while the former is ~ 20 MeV at RHIC and close to zero at LHC, which is expected given that μ_B decreases as a function of energy.

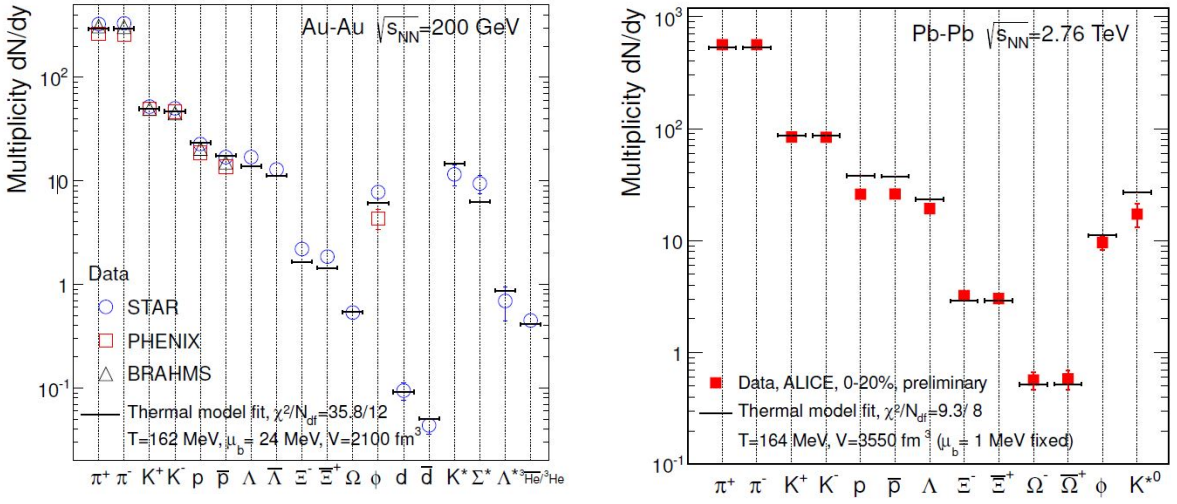

(a) (b)

Figure 1.6: Comparisons of thermal model calculations with RHIC data in central Au-Au collisions (a) and ALICE data in central Pb-Pb collisions (b).

Furthermore, as expected, there is an enhancement in the production of multi-strange hadrons (Ξ and Σ) which is also underpredicted both at RHIC and at LHC (even though to a lesser extent).[16]

1.4.2 Elliptic Flow

Collisions at ultra-relativistic speed inside colliders produce a very large number of subatomic particles moving in all directions. When the nuclei collision is not central, the initial matter distribution is anisotropic. Given that the partonic matter is strongly interacting, this spatial asymmetry in the subatomic particles trajectories can be converted through multiple collisions into an anisotropic momentum distribution. Hence

the azimuthal distribution (considering the angle ϕ), will not be uniform. An expansion in a Fourier series yields

$$\frac{\mathrm{d}n}{\mathrm{d}\phi} = 1 + 2v_2(p_\mathrm{T})cos(2\phi) + \dots$$

where the coefficient v_2 represents the *elliptic flow*, which is a measure of how the flow is not uniform in all directions when observed along the beam axis and it is a strong evidence for the existence of QGP. For this reason it has been studied extensively at RHIC and also at LHC, using higher energy.
The theoretical predictions from hydrodynamic models describe well most of the measurements of the elliptic flow of light hadrons at p_T lower than $\sim$ 2-3 GeV. Moreover the measurements taken at RHIC and LHC show that the created matter equilibrates in an early stage of the collision (so after a short time particles ratios are fixed); they show that the hot matter evolves following hydrodynamics laws and that it behaves like a perfect fluid (as supposed by hydrodynamic model), too.
RHIC results were confirmed by measurements at the LHC collider, where the elliptic flow is being studied in much more details and in a wider momentum range (up to p_T $\sim$ 60 GeV).
In the following pictures (Fig. 1.7 and Fig. 1.8) a compilation of results from both colliders are shown[14].

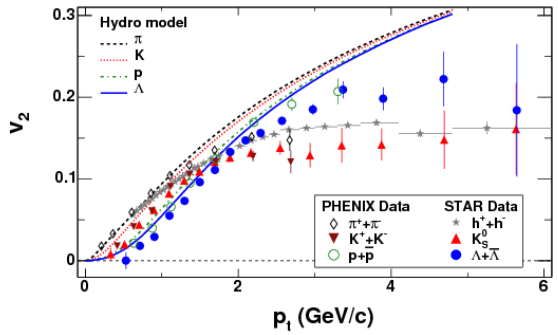

Figure 1.7: Elliptic flow v_2 as a function of the transverse momentum p_T at RHIC.

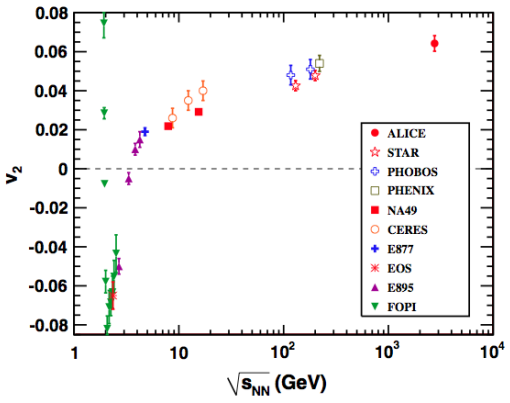

Figure 1.8: Elliptic flow v_2 as a function of the energy per nucleons pair colliding in the center of mass at RHIC, LHC and other experiments.

1.4.3 Jet Quenching

Generally, collisions of high-energy particles create *jets* of elementary particles, which are composed of hadrons produced by hadronization of quarks and/or gluons.
At ultra-relativistic speed heavy-ion particle beams may create QGP (*fireballs*) with whom these jets can interact strongly, leading to a remarkable reduction of their energy through *bremsstrahlung* (a deceleration radiation). This energy reduction is called *jet quenching*.
Experimentally, if two jets are observed (*dijets*), a striking imbalance in energy should be seen between them due to an energy absorption of one of the jets by the medium. For this reason signals with high p_{T} can be used as probes for studying QGP characteristics. Hadron azimuthal correlation $\Delta\phi$ is used to highlight the quenching.
At RHIC first experiments were made with p+p collisions, secondly with d+Au collisions, where d is the deuteron (the nucleus of deuterium) formed by a proton and a neutron, and lastly with Au + Au collision, but only with Au + Au collisions a suppression was found. For this reason *jet quenching* is regarded as a signal of QGP creation. At LHC for $Pb + Pb$ collisions a much smaller suppression is seen, because energy is much larger, and observable reduction is not so simple to notice.
However an increase of energy near the jet at $\Delta\phi = \pi$ is observed, meaning that, for the conservation of kinetic energy, hadrons from the medium interacting with the jet are revealed at different angles.[17]
Fig. 1.9 and Fig. 1.10 show data respectively collected at RHIC, at different associated p_{T} and with different centrality, and at the LHC, with constant transverse momentum.

[9]PYTHIA simulates p+p collisions, while HIJING simulates nuclei collisions.

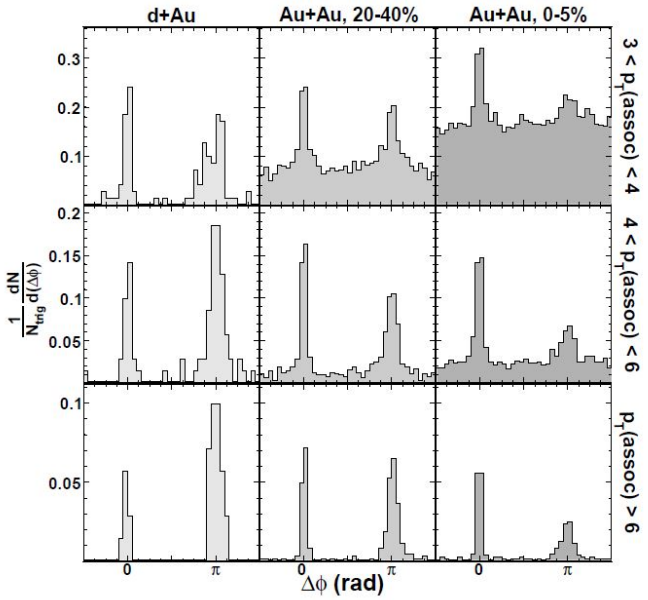

Figure 1.9: Azimuthal correlation of charged hadrons in different p_{T} ranges as a function of $\Delta\phi$, the azimuthal angle between 2 jets, at RHIC for d-Au and Au-Au collisions at (20-40)% and (0-5)% centralities. As predicted one of the two peaks of the dijet is impressively suppressed in central collisions.

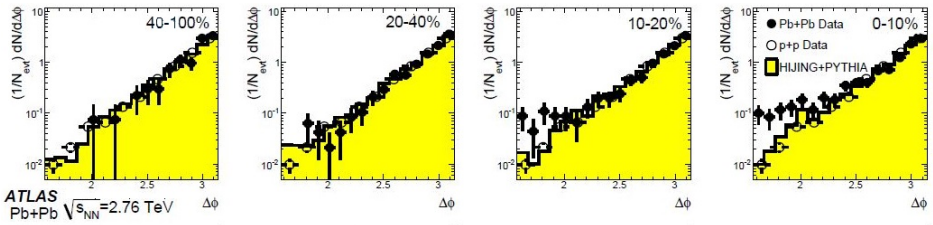

Figure 1.10: Azimuthal correlation of charged hadrons with high fixed p_{T} of ~ 100 GeV as a function of $\Delta\phi$ at LHC. Proton-proton data are shown as open circles, besides solid yellow histograms show simulation from HIJING and PYTHIA[9]. The distribution also depends on the centrality (left to right from peripheral to central events). An asymmetry in Pb+Pb collisions can be observed, due to the interaction of hadrons with the medium that causes a deviation in jets trajectories from π.

Chapter 2

ALICE: A Large Ion Collider Experiment

ALICE is one of the LHC experiments and it has been designed and optimized to measure particles produced in nuclei collisions using heavy ions (Pb+Pb) with $\sqrt{s_{NN}} = 5.5$ TeV. To detect the multitude of particles created by collisions many different detectors are needed, whose constructions took almost a decade, because in some cases the needed technology had to be developed during their construction.
Moreover, to analyze the physics variables of interest, PID (*Particle IDentification*) is also important, whose principles will be described later.[15]

2.1 ALICE detectors

In heavy ions collisions the multiplicity of produced particles is much larger than in p-p collisions. For this reason detectors were designed to optimize the acceptance and detection efficiency in a very high multiplicity scenario.
ALICE consists of a central part which detects hadrons, electrons and photons and a forward spectrometer to measure muons. The former covers a polar angle of $\pm 45°$ (a pseudorapidity range $|\eta| < 0.9$) over the full azimuthal angle.
In the central part there is also a solenoidal magnet, that creates a constant homogeneous magnetic field B = 0.5 T, needed for the momentum measurement.
Outside of the magnet, besides the muon spectrometer and at high distance from the central detector, there is also a set of small calorimeters used to measure the collisions impact parameter[1](Zero Degree Calorimeter [**ZDC**]).
Fig. 2.1 shows ALICE with its individual components, some of which will be described in the next sections.

[1]The impact parameter b is defined as the distance between the centers of the two colliding nuclei in the plane transverse to the beam axis.

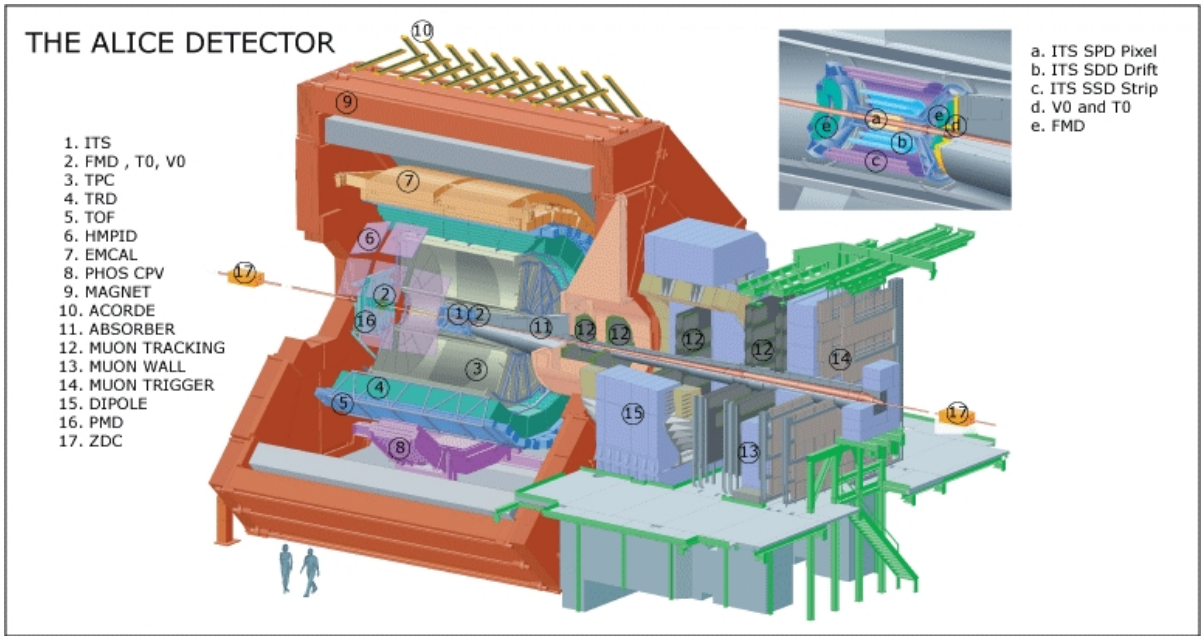

Figure 2.1: ALICE with its detectors. Two people are portrayed to show better the dimensions of the apparatus which is: 26 m long, 16 m high and 16 m wide, with a mass of approximately 10^4 tons.[19]

2.1.1 Inner Tracking System (ITS)

The ITS consists of six cylindrical concentric layers of silicon detectors coaxial to the beam. These layers surround the collision point and measure the trajectories of the particles emerging from it.
As for the TPC, this detector can identify charged hadrons with a $p_T < 1$ GeV/c.
The ITS layers, as can be seen in Fig. 2.1, are (from the inner to the outer region):

- 2 layers of Silicon Pixel Detector (*SPD*),
- 2 layers of Silicon Drift Detector (*SDD*),
- 2 layers of Silicon Strip Detector (*SSD*),

where the innermost four layers are two-dimensional devices, due to high particle density.[15]
The main goals of this detector are:

- primary and secondary vertices reconstruction, achieving a resolution on the primary vertex lower than 100 μm, while secondary vertices reconstruction is required for charm and hyperon decays;
- tracking of low-momentum charged particles ($p_T > 100$ MeV/c);
- measurements of low-energy particles momentum and particle identification through ionization energy loss dE/dx, done by the 4 outermost layers;

- improvement of the momentum resolution, in combination with the TPC.

2.1.2 Time Projection Chamber (TPC)

The **TPC** is the principal tracking system in ALICE; it measures momentum and identifies particles using $\frac{dE}{dx}$, which is their specific energy loss. It has a high efficiency in track finding for up to 12000 charged particles (for example kaons, pions and protons) within the acceptance.
The inner radius of the detector is 85 cm, given by the maximum acceptable tracks density that is $0.1/cm^2$, and the outer one is 250 cm, required for an energy loss resolution $< 10\%$, resulting in a total sensitive detector volume of 88 m^3.[15]
The apparatus is filled with a gas mixture of Ne-CO_2 (90:10) that allows to reduce multiple scattering effect, thanks to a low diffusion parameter and a high radiation length, and let the TPC to be used for PID with a 3σ separation, with a momentum lower than 1 GeV/c, thanks to a significant particles loss of energy even at high momentum.
Tracks reconstruction begins from outer regions, where density is lower, to inner ones, which are much more influenced by tracks proximity (sometimes they even overlap).
TPC works together with ITS; as a matter of fact 10% of tracks are not detected in the TPC, because of the "dead zones" among sectors and decays, while they're reconstructed by the ITS.

2.1.3 Transition Radiation Detector (TRD)

The **TRD** is the main electron detector in ALICE. It identifies electrons with a momentum > 1 GeV/c in the central region of ALICE, while those with lower momentum are identified by energy loss measurements in TPC.
The TRD consists of 522 chambers arranged in six layers surrounding the TPC at a radial distance $2.9 \leq r \leq 3.7$ m, with a maximum lenght of 7 m along the beam axis (this leads to a pseudorapidity coverage of $|\eta| < 0.9$). Including a 4.8 cm thick radiator, *front-end* electronics and cooling system, one chamber has an average size of 135 cm x 103 cm and is ~ 12 cm thick.
Each chamber is filled with a mixture of Xe-CO_2 (85:15). Its volume is subdivided by a catode wire grid into a 3 cm drift region and a 0.7 cm amplification region equipped with anode wires. The induced signal on the cathode plane is normally spread over some pads, which are rectangular and have an average area of about 6 cm^2.
In conjunction with both TPC and ITS, it provides the necessary electron identification capability to study the production of light and heavy mesons. The former, as already said, are important because they decay in charged leptons pairs and in quarkonium states ($c\bar{c}$ and $b\bar{b}$) and the latter, coming directly from interaction region, can be distinguished from those obtained by heavier particles decays using ITS measurements of secondary vertices.
Moreover the TRD can be used to trigger on identified particles with high momenta, thus providing enriched samples of different probes (i.e. single electrons or electron-positron

pairs), and it allows also to select jets.[20]

2.1.4 Particle identification systems

Three detectors in ALICE are completely dedicated to particle identification:

- The Time Of Flight (TOF), used for the measurements of the time of flight of charged particles with intermediate ([0.5-1]GeV) p_T (it will be described more in detail in the next chapter);

- The High Momentum Particle Identification Detector (HMPID) which is dedicated to high p_T hadrons detection. This is a RICH detector (Ring Imaging Cherenkov detector) located at 4.9 m from collision zone, it is divided in seven modules, covering an active region of about 10 m^2.
  The HMPID has been designed to extend the useful range for the identification of particles beyond ITS, TPC and TOF momentum range limit.
  When charged particles with high speed go through the detector, Cherenkov photons are emitted and they are detected by a photons counter which use a thin layer of CsI (Caesium Iodide) deposited onto the pad cathode of a multiwire proportional chamber (MWPC)[15];

- The Photon Spectrometer (PHOS) is a high resolution electromagnetic calorimeter from which informations about thermal and dynamical properties of collisions during their initial phase can be obtained, using photons spectra.
  It has 17920 detection channels based on lead-tungstate crystals ($PbWO_4$) with an operating temperature of -25 °C, covering an area of 8 m^2. These are necessary to detect direct photons, whose study is important because a production increase of photons with $p_T > 2$ GeV/c should be seen in QGP rather than in normal hadronic matter.

2.2 Time-Of-Flight (TOF)

2.2.1 System description

The detector has a cylindrical shape and it covers polar angles from 45 to 135 degrees over the full azimuthal angle ϕ. The inner radius is 3.7 m and the complex is long 7.4 m.
The apparatus has a modular structure with 18 sectors in ϕ, each having 5 modules along the beam direction, for a total of 90 modules (see Fig. 2.2).
These contain a total of 1638 Multigap Resistive Plate Chamber strips (which are detectors), covering an area of 160 m^2 with 157248 readout channels (pads).
Each sector contains a super module, which is a group of 5 modules:

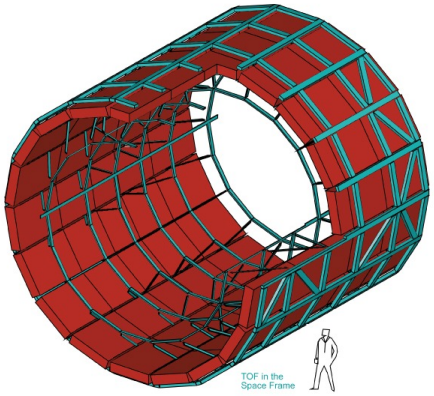

Figure 2.2: TOF overall structure.

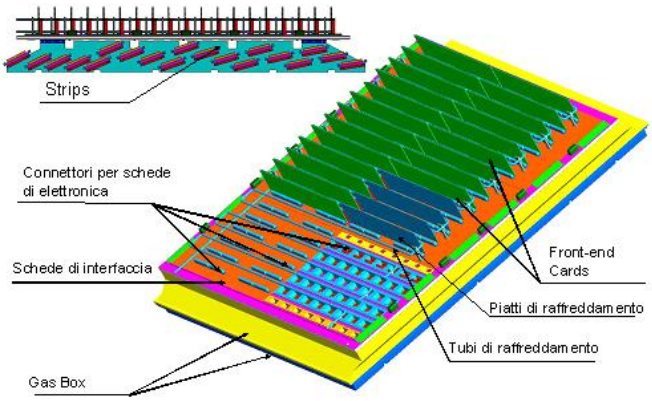

Figure 2.3: Scheme of a TOF module.

- 1 inner module containing 15 MRPC and having a lenght of 1.14 m;
- 2 intermediate modules each containing 19 MRPC and having a length of 1.47 m;
- 2 external modules each containing 19 MRPC and having a length of 1.78 m;

Each module is divided into two regions, an inner one, made by fiber glass, containing gas, which is a mixture of freon ($C_2H_2F_4$), isobutane (C_4H_{10}) and sulfur hexafluoride (SF_6) [90:5:5], where MRPC are located, and an outer one containing *front-end* electronics connected to *readout* modules through variable length wires.
A graphic scheme of a TOF module can be seen in Fig. 2.3 [15].

Multigap Resistive Plate Chamber (MRPC)

The MRPC is a stack of resistive glass plates and a high voltage is applied to its external surfaces. Further out there are pickup electrodes.
The fundamental physical process of this kind of detectors is particles ionization. A charged particle, during its movement, ionizes the gas (producing an ion-electron pair) and the high electric field amplifies this ionization leading to an electron avalanche (if the produced pair has sufficient energy after the acceleration made by the electric field), whose development is stopped by the resistive plates in each gap.
If the potential difference between the electrodes is sufficiently high, a *streamer* will be originated from primary and secondary avalanches, which is a quicker conductive channel compared to the avalanche processes speed. Finally, when electrons and ions reach both electrodes, a *spark* is created.
The MRPC are an evolution of RPC (*Resistive Plate Chambers*), motivated by the necessity of a new kind of detector with an extremely good time resolution, and with the possibility to sustain frequencies of the order of some hundreds of Hz/cm^2 and which can maintain a low current inside the gas having, at the same time, a good output signal.
In the detector the gap (which is the space between anode and cathode) is divided by

various resistive parallel plates, creating a series of *gas-gap*, thanks to whom the development of avalanches is shorter, but the probability of having *streamer* increases, giving high gain and maximum time resolution.
The final stage of the detector development is the double stack MRPC, which are essentially two parallel connected MRPC with a common central electrode. Therefore having more *gaps* leads to almost unit efficiencies and excellent time resolutions without the need of high tensions.
Readout electrodes are segmented into pads and located in PCBs (Printed Circuit Boards). To make the system more rigid two *honeycomb* panels are attached to the two most external PCBs.

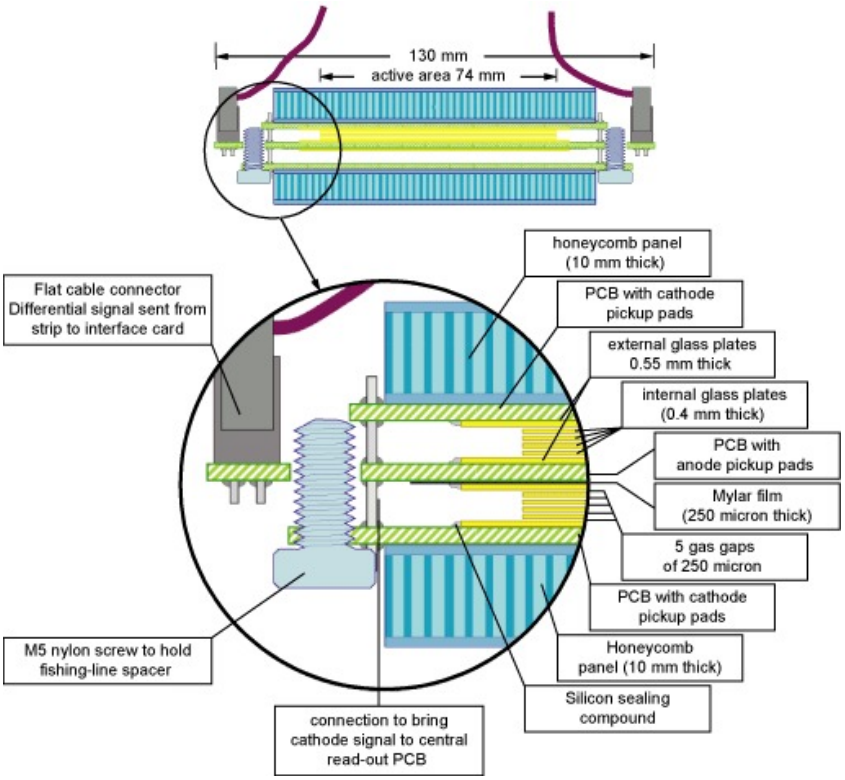

Figure 2.4: Schematic transversal section of a double stack MRPC

Each long MRPC strip of TOF has an active area of 7.4 x 120 cm^2; it has 96 readout pads of 2.5 x 3.5 cm^2 arranged in two rows; it consists of 2 stacks of glass each with 5 gaps of 250 μm and spacers made of nylon fishing line to keep the distance among the 4 internal resistive glass plates.
Moreover, it has two external glass plates covered by acrylic paint with a superficial resistance of 5 MΩ, which are 550 μm thick (see Fig. 2.4).
The double stack configuration has numerous advantages compared to a single stack MRPC:

- given that the measured signal is the sum of the two stacks (in each MRPC is the sum of the signals from all gaps), the output itself is amplified by a factor of 2;
- the applied tension is halved;
- it is possible to reduce the distance between anodic and cathodic planes to lower the dimension of avalanche print, obtaining a more precise distinction of the signals on the pads.

2.2.2 Particle Identification (PID)

A particle is identified when its charge and its mass are known (in stability conditions). The mass is determined by independent measurements of two kinetic observables, where one of these must not depend on mass.
TOF has the task to identify charged hadrons (π, K, p) with $0.5 < \mathrm{p}_T < 2.5$ GeV/c for π and K and up to 4 GeV/c for p (beyond the limits of the energy loss measurements in ITS and TPC).
In this interval the time resolution needed to have a separation of 3σ of charged hadrons must be lower than 100 ps. For this reason MRPC are designed to have a time resolution lower than 50 ps and efficiencies of 99.9%. Dedicated *front-end* and *readout* electronics had to be developed to optimize detectors performances.
With a TOF detector it is possible to measure the speed (v) of the particle passing through the detector itself, using the time of flight (t) that the particle takes to travel a known distance L.
The mass can be found from the velocity v and the momentum p using the relativistic relation:

$$\begin{aligned} m &= \frac{p}{c}\sqrt{\frac{1}{\beta^2} - 1} = \\ &= \frac{p}{c}\sqrt{\frac{t^2c^2}{L^2} - 1} \text{ with } \beta = \frac{v}{c}. \end{aligned} \tag{2.1}$$

The TPC has the task to find the momentum p of the particle, which is used to calculate the mass through the Eq. 2.1.
Moreover the ability to distinguish two particles in a TOF detector is given by

$$n_{\mathrm{d}t,1-2} = \frac{Lc(m_1^2 - m_2^2)}{2p^2\mathrm{d}t},$$

where $n_{\mathrm{d}t,1-2}$ is the separation between two times of flight in terms of standard deviation σ.
The particles charge can be found using a magnetic field that bends particles trajectories. They will tend to have an helical path with a fixed radius of curvature (R) depending

on the magnetic field strenght (B) and on particle momentum (p).
This leads to the following relation

$$p = qRB\,,$$

where q is the charge of the particle.

2.3 PID Performance

The detector systems used to identify hadrons in ALICE are TOF, ITS, TPC and HMPID, whose functions have been previously described.
The different detectors measurements are eventually combined to improve the separation among particle species.

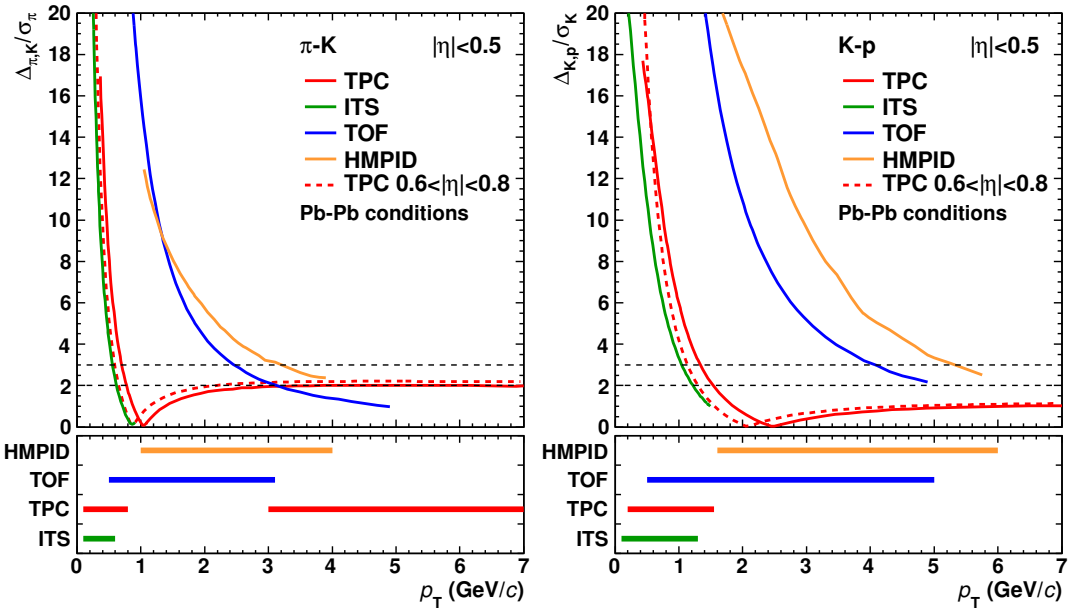

Figure 2.5: Separation power of hadron identification in the ITS, TPC, TOF and HMPID as a function of the transverse momentum at mid-rapidity, which means $|\eta| < 0.5$. The left panel shows the separation of pions and kaons, while the right one shows the separation of kaons and protons. Both are expressed as the ratio of the distance between the peaks of the particle pairs to the resolution for the pion and the kaon, and for the kaon and the proton, respectively. In the top plots an additional curve for the TPC is also shown in the region $0.6<|\eta|<0.8$. The bottom plots instead show the range over which the detector systems have a separation power higher than 2σ.

The plots in Fig 2.5 show that the detection systems are complementary. In point of fact at low $p_T < 500$ MeV/c the TOF and HMPID are not efficient, so TPC and ITS provide the main separation, while at intermediate p_T, TOF and HMPID provide more than 3σ

separation power, but the former is efficient up to 3 GeV/c for pions or kaons and 5 GeV/c for protons, while the latter is efficient respectively up to 4 GeV/c and 6 GeV/c. The TPC can also be used to separate pions from protons and kaons at higher p_{T} with a $\sim 2\sigma$ separation and, in addition, protons and kaons can be separated statistically with a multi-Gaussian fit to the collected signal.
Moreover combining the information from multiple detectors can further improve the separation [15].

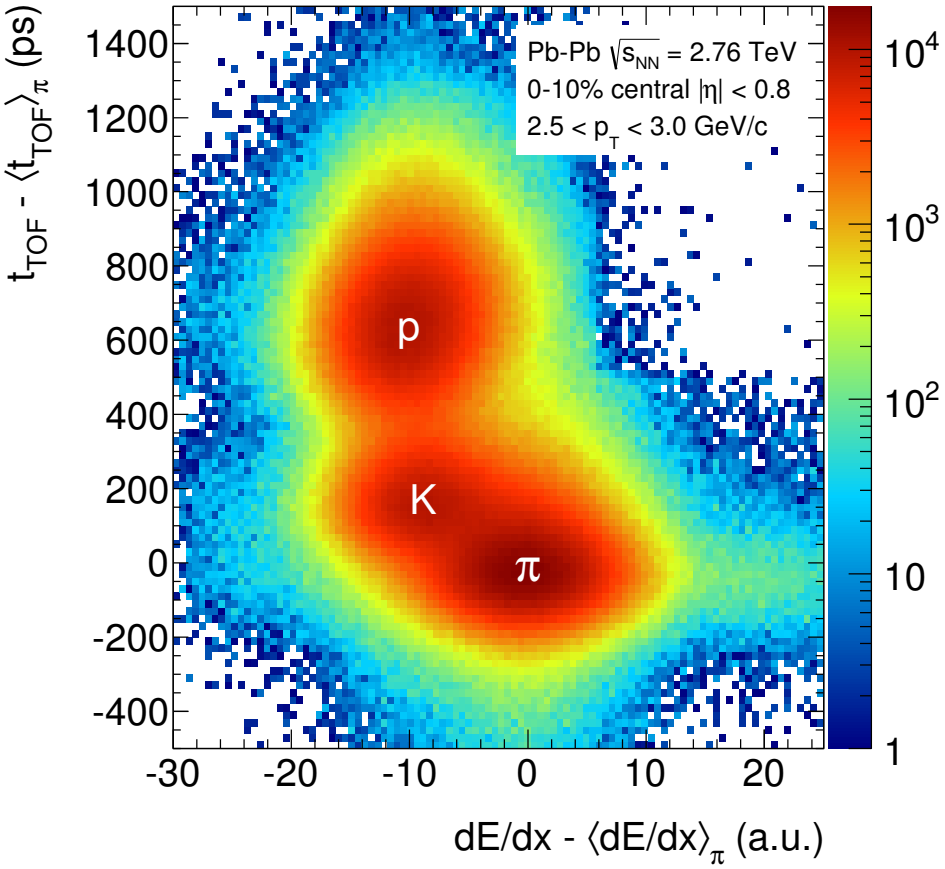

Figure 2.6: Combined pion identification with TOF and with the ionization energy loss (dE/dx) in the TPC.

2.4 Bayesian PID

The Bayesian approach can be used to combine PID over several detectors; in fact simple selections based on individual PID signals of each detector do not take full advantages of the particle identification capabilities of ALICE.

Hence to maximize the PID capabilities of ALICE a Bayesian approach has been implemented. Using this approach, for a single detector can be defined a conditional probability r(s|i) to observe in some detector a PID signal s if a type i particle is detected, where i=$(e, \mu, \pi, K, p \dots)$. It is then necessary to fold the probabilities with *priors*, which are particles expected abundances.[22]
In fact, using priors C_i, the probability w(i|s) that given an observed signal s the particle detected will be of i-type can be calculated using the bayesian relation:

$$w(i|s) = \frac{r(s|i)C_i}{\sum_{k=e,\mu,\pi,K,p\dots} r(s|k)C_k} \,. \tag{2.2}$$

After determining a detector response function, according to which an r(s|i) value is assigned to each track, a-priori probabilities are estimated from a subset of events and tracks selected in a specific physics analysis.[23]
The most simple condition is when all priors are set equals, but they can be found more precisely using data coming from different detectors.
The same thing can be done using multiple detectors and calculating the combined response function P($\vec{s}$|i) which is the product of the single response functions:

$$P(\vec{s}|i) = \prod_{\alpha=ITS,TPC,\dots} r_\alpha(s_\alpha|i) \,, \tag{2.3}$$

where $\vec{s}$=(s_{ITS},s_{TPC},$\dots$).
Afterwards, as before, a W(i|$\vec{s}$) probability can be calculated, using the same formula as for w(i|s), but with P($\vec{s}$|i) replacing r(s|i).
Priors are a *best guess* of the true particle yields per events and they can be also used to reject certain particle species that are not relevant to a given analysis.
PID efficiencies, useful to obtain the physical quantity of interest from a raw yield, can be evaluated using Monte Carlo simulations, which need an accurate description of the actual signals in the data.
These simulations need also priors, whose choice is really important because if they lie closer to the true abundances, the best compromise between the maximization of the efficiency and the minimization of the contamination[2] probabilities will be found.
When the Bayesian probability for each particle species has been calculated for a given track the particle identification selection can be applied using various criteria, like using the maximum probability to define the particle species or requiring that the probability is larger than a given threshold to accept the track as a given species.

[2]That is

$$c_{ji} = \frac{N_{i \text{ identified as } j}}{A^j_{meas}}, \tag{2.4}$$

where the numerator is the number of particles belonging to species i that are wrongly identified as j, whereas the denominator is the total number of identified j particles.

Chapter 3

Λ_c detection

In this section the Particle IDentification (PID) performance for the detection of the Λ_c charmed baryon, whose quark composition mass and width are reported in Table 3.1, reconstruction using the Bayesian approach is presented.

Λ_c		
Quark content	**Mass (MeV/c^2)**	**Mean lifetime (10^{-15} s)**
udc	2286.46 ± 0.14	200 ± 6

Table 3.1: Λ_c properties.

The Bayesian PID will be compared with other particle identification methods used in ALICE, which will be described in the next sections.
ALICE has already measured the charm quark suppression at high p_{T} through D mesons [30]. Hence the study of the Λ_c production in PbPb collisions is important because it allows to investigate the recombination processes, as already done in the case of strange quarks using the ratio Λ to K [25].
The Λ_c particle has a large number of *decay modes* (listed in Fig. 3.1 in the case of the hadronic channels). In this thesis the πKp channel was studied, since it is one of the channels with the highest probability for the particle decay ($\approx 6.84\%$).

3.1 Fast simulation

In order to evaluate the PID performance and the achievable significance for Λ_c detection in ALICE using RUN2 and RUN3 statistics, a Fast Simulation was developed.
The particle simulation program allows to generate a cocktail of Λ_c signals and PbPb collision events with different weights.
A fast simulation is used instead of a full one, because the latter is much slower and could be used to study more deeply the new approach if the fast simulation shows that the

Mode		Fraction (Γ_i / Γ)
Hadronic modes with a p: $S = -1$ final states		
Γ_1	$p\overline{K}^0$	$(3.21 \pm 0.30)\%$
Γ_2	$pK^-\pi^+$	$(6.84^{+0.32}_{-0.40})\%$
Γ_3	$p\overline{K}^*(892)^0$	$(2.13 \pm 0.30)\%$
Γ_4	$\Delta(1232)^{++}K^-$	$(1.18 \pm 0.27)\%$
Γ_5	$\Lambda(1520)\pi^+$	$(2.4 \pm 0.6)\%$
Γ_6	$pK^-\pi^+$ nonresonant	$(3.8 \pm 0.4)\%$
Γ_7	$p\overline{K}^0\pi^0$	$(4.5 \pm 0.6)\%$
Γ_8	$p\overline{K}^0\eta$	$(1.7 \pm 0.4)\%$
Γ_9	$p\overline{K}^0\pi^+\pi^-$	$(3.5 \pm 0.4)\%$

Figure 3.1: Hadronic branching ratios of the Λ_c [26].

method is actually better than the others. As a matter of fact with the fast simulation an estimate will be given of how much the approach is more efficient compared to the others within the condition that have been set up to perform this study.
The simulation parameters are tuned on PbPb collisions at 5.02 TeV with centrality 0-20%. Using the *Glauber model*[1] and the data obtained by ZEUS for Λ_c production [27], the number of particle per event and unit of rapidity was calculated:

$$(600\,\mu\text{b}) \cdot \frac{1.44}{72\,\text{mb}} \cdot 1340 \cdot 0.118 \cdot 0.4 = 0.76\,. \tag{3.1}$$

In Eq. 3.1, 600μb (value taken from FONLL computation [28]) is the differential $c\bar{c}$ cross section at mid rapidity in pp collisions at 2.76 TeV, 1.44 is the energy scaling factor, obtained from the ratio between the $c\bar{c}$ total cross sections at 5.02 and 2.76 TeV in pp collisions (which are respectively 6.9 mb and 4.8 mb [29]), 72 mb is the inelastic nucleon-nucleon cross section for PbPb collisions at 5.02 TeV, 1340 is the mean value of binary collisions at 0-20% centrality, obtained from the values of the Glauber Monte Carlo listed in Table 3.2, 0.118 is the fragmentation function $f_c \to \Lambda_c$ predicted by the thermal model [27], which is also consistent with the results obtained by ZEUS, and 0.4 is the nuclear modification factor R_{AA}, as measured for the D mesons (which are the lightest particles containing charm quarks) in PbPb collisions at 2.76 TeV [30].
In the simulation, the performance at both the TOF and the TPC detectors are taken into account. The reconstruction efficiencies of the detectors, shown in Fig 3.2, were

[1]The Glauber model allows to calculate relevant quantities in particle collisions physics, like the impact parameter (b), the number of participating nucleons (N_{part}) and the number of binary nucleon-nucleon collisions (N_{coll}). [24]

Centrality	Npart	Ncoll
0-5%	384.5	1875.9
5-10%	333.1	1464.4
10-15%	284.4	1146
15-20%	241.5	893.3
20-25%	204.2	692.1

Table 3.2: Glauber Monte Carlo predictions for the number of participating nucleons (N_{part}) and the number of binary nucleon-nucleon collisions (N_{coll}) in PbPb collisions at 5.02 TeV [31].

simulated via parameterizations based on both Monte Carlo and real data. Their dependence as a function of the transverse momentum of the track is shown in Fig. 3.2. After a threshold behaviour due to the magnetic field and the effect of the interaction of the particles with the detector material, the TPC and TOF efficiencies saturate at 0.9 and 0.7 respectively, for $p_{\mathrm{T}} \gtrsim [0.5 - 1]$ GeV/c.

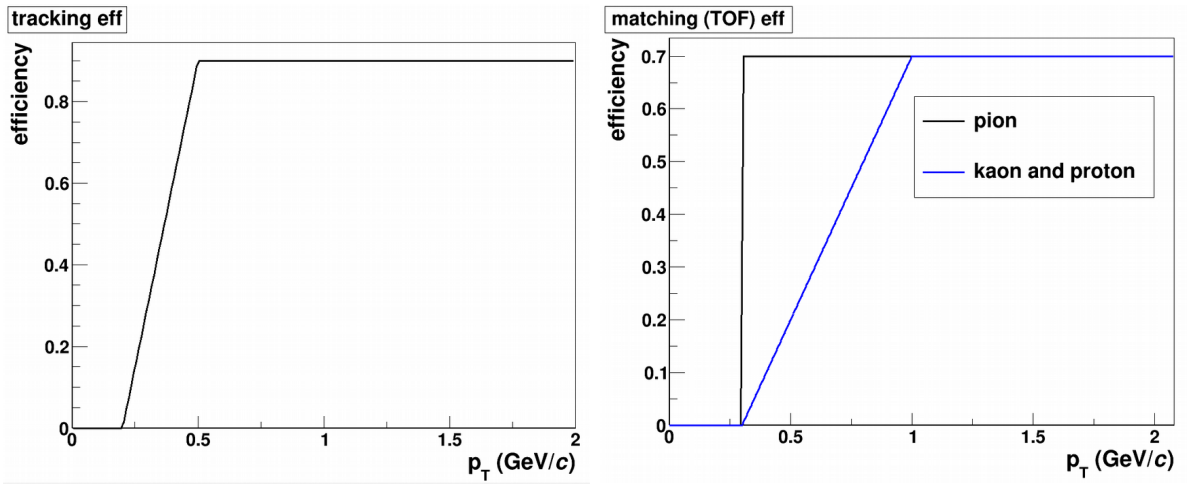

(a) (b)

Figure 3.2: Tracking efficiencies for TPC (a) and TOF (b) as a function of the transverse momentum p_{T}. In the former all the particles saturate at 0.5 GeV/c, instead in the latter pions saturate at $\approx$ 0.3 GeV/c, while kaons and protons saturate at 1 GeV/c.

The invariant mass distribution of the Λ_c is simulated around the nominal value M_{Λ_c}=2286.46 $\pm$ 0.14 MeV/c^2 as a Gaussian having a width of 8 MeV, which represents the current detector resolution achieved for this channel in pp collisions. The contribution of the Λ_c natural width is negligible.

Moreover, PbPb events with centrality 0-20% were simulated assuming π, K, p abundances and p_{T} distributions accordingly to the ones measured by ALICE at 2.76 TeV, with multiplicity scaled by a factor 1.2 to take into account the increased multiplicity at 5.02 TeV [32].
The π, K, p were analyzed within an acceptance of $|\eta| < 0.9$. The software simulated the particles separation for TPC and TOF according to the performance reported in Fig. 2.5.

3.1.1 Expected statistics

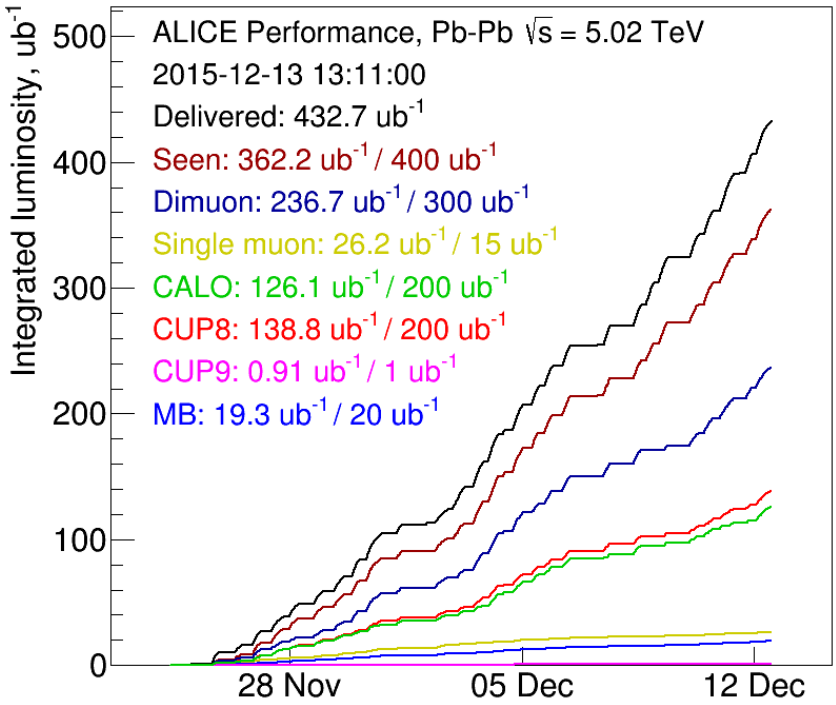

Figure 3.3: Expected statistics for different triggers at LHC. The plot corresponds to the values of the RUN2.

Two values of the expected statistics of events selected by the Minimum Bias trigger (**MB**), where considered in this study:

1. **RUN2**: the integrated luminosity is for MB $\approx 20\,\mu\mathrm{b}^{-1}$, that means 30 millions of events for PbPb collisions with centrality 0-20% at 5.02 TeV, as Fig. 3.3 shows;

2. **RUN3**: the expected integrated luminosity is $\approx 10\,\mathrm{nb}^{-1}$, which corresponds to 15 billions of events for PbPb collisions with centrality 0-20% at 5.02 TeV.

3.2 PID approaches comparison

In parallel with the analysis based on the weighted Bayesian approach, two other methods were used to analyze the data from the Monte Carlo simulation. Since the Monte Carlo data contain also the information about the number of the true Λ_c that have been generated, a study on which approach is the most efficient can be made.

3.2.1 *Cuts* approaches

The following PID methods are largely used in ALICE and for this reason they were chosen for the comparison with the weighted Bayesian approach.

Nσ cut

The particle selection has been applied by requiring a 3σ cut on the signal distribution around the expected value for a given mass hypothesis. This means that the fraction of signal accepted by this approach is, by definition, $\approx 99.7\%$.
Unfortunately the use of this cut yields to high values of background and, consequently, this limits the significance of the measured signal, which is defined as:

$$Significance = \frac{S}{\sqrt{S+B}}\,, \tag{3.2}$$

where S is the measured signal and B the background below the 3σ signal.

Standard Bayesian cut

The selection via a cut on the Bayesian probability (described in section 2.4) is another frequently used approach for particle identification in ALICE.
Using the known particle abundances, already measured by ALICE in *pp* collisions, it was possible to guess the function of the priors, depending on the transverse momentum p_{T}[2].
The abundances for PbPb collisions might be different from those of *pp* collisions, but the difference is expected to affect the results presented here in a negligible way. For the reconstruction of Λ_c, the fundamental characteristics of the priors functions must be:

1. *Pions* are the most abundant, on the basis of our knowledge, within the momentum interval analyzed and their distribution is constant by definition;

2. *Kaons* have an abundance that starts from 0 and reaches 0.4 for $p_{\mathrm{T}} \to 10$ GeV/c (which is the limit of the interval analyzed);

3. *Protons* have priors similar to kaons, but the abundance reaches 0.2.

[2]Prior abundances are conventionally defined as a ratio with respect to pions.

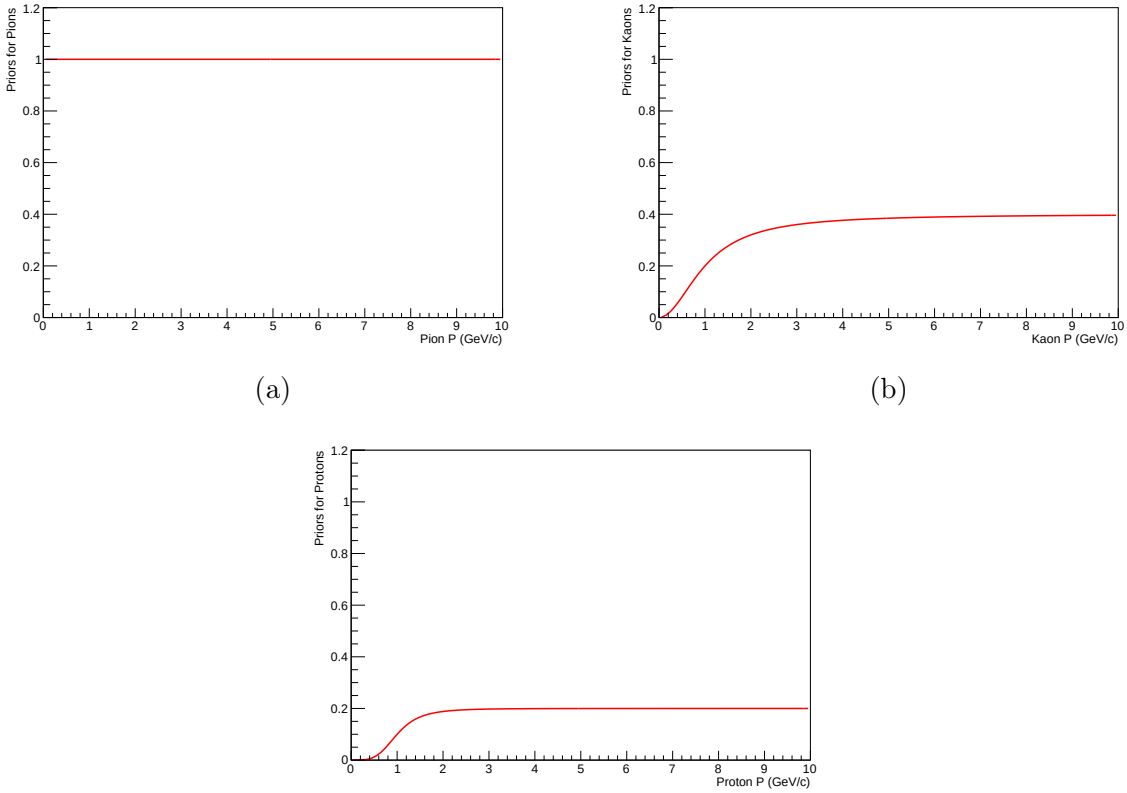

(a) (b)

(c)

Figure 3.4: Priors functions used for the three kinds of particle: (a) Pions, (b) Kaons and (c) Protons, as a function of the particle transverse momentum p_{T}

Given these premises, the priors functions used for the approach were computed and they are shown in the plots of Fig. 3.4.
The Bayesian probability is computed track by track as in Eq. 2.1 and a track is accepted for a given mass hypothesis if the corresponding probability is larger than 30%.

3.2.2 *Weighted* Bayesian approach

To improve the PID performance a new method based on the Bayesian approach was explored. The new method replace the cut on the Bayesian probability with weights. In practice the Bayesian probability is no longer used to decide whether a particle belongs or not to a given species but it is actually used as a probability to weight histograms. In this way all the tracks are accepted in the analysis and if the priors are tuned properly the method should be very close to the case of perfect PID at the statistical level. Therefore this new approach should be the most efficient compared with the other two.
The optimal tuning of priors can be achieved using an iterative procedure which takes as input priors at a given step the abundances measured in the previous step (starting

from equal priors assumption at step-0). In the case of the Λ_c in the πKp channel, the probability can be generalized for a triplet. So the probability for any combination of mass hypotheses is defined for each triplet using a set of 27 (3x3x3) priors for all the possible combination, as:

$$P^{ijk}(\vec{S}) = \frac{p_i(S_1)p_j(S_2)P_k(S_3)C_{ijk}}{\sum_{m,n,o} p_m(S_1)p_n(S_2)P_o(S_3)C_{mno}}\,, \tag{3.3}$$

where p(s) is the detector response function, i.e. the probability density that a given species realizes the measured signal S. In Fig. 3.5 results of the procedure are shown within different p_{T} intervals of the Λ_c, after 20 steps and compared to the perfect PID case.
As it can be noted this new method allows to reject all the background from misidentification and to reconstruct almost all the signal depending on the kinematic region under consideration.

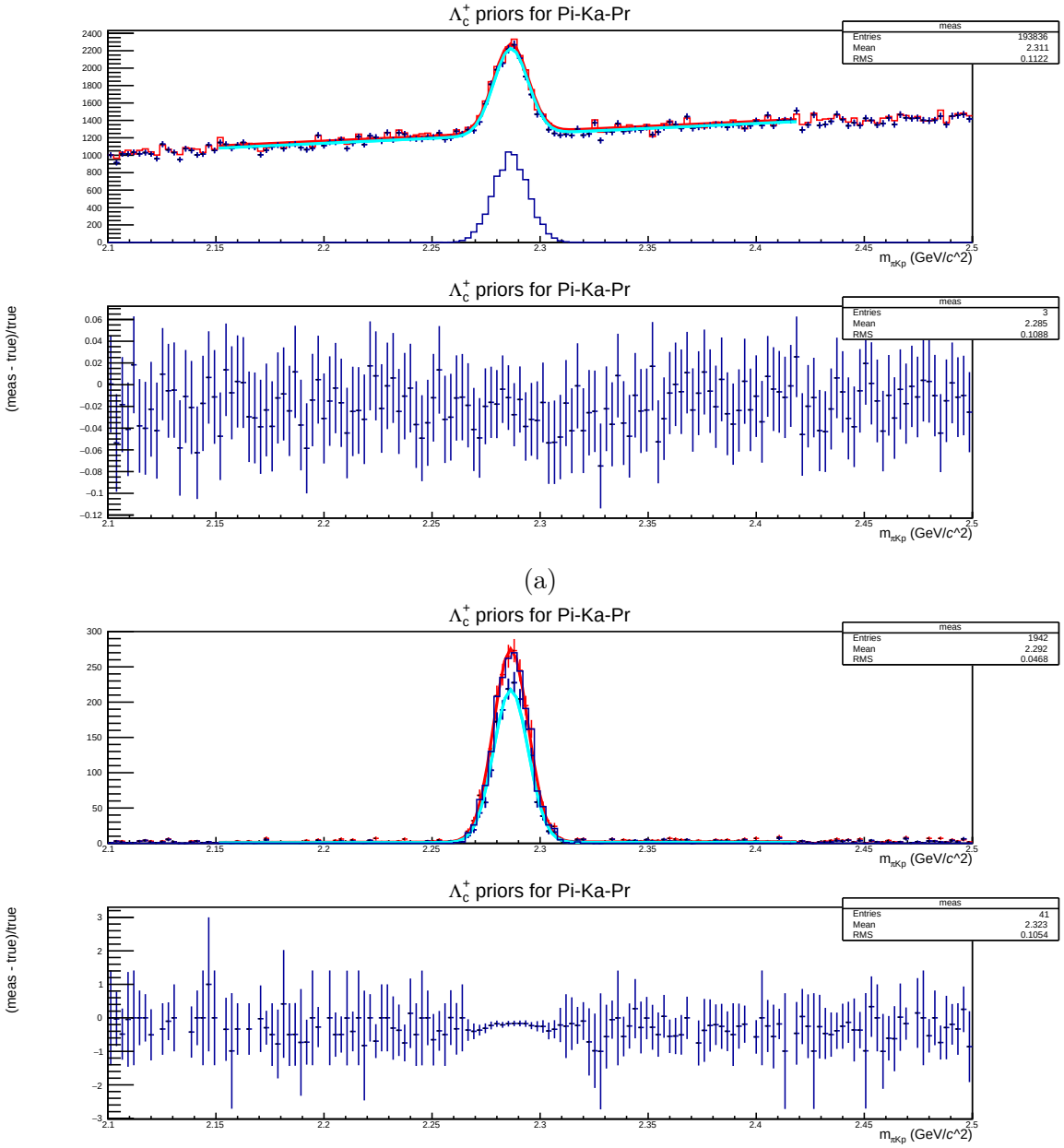

(a)

(b)

Figure 3.5: Λ_c detected as a function of the invariant mass $m_{\pi Kp}$ of the πKp triplet for the intervals of momentum 2-7 GeV/c and 7-10 GeV/c (top graphs of (a) and (b) respectively), and $\frac{\Lambda_c^{measured} - \Lambda_c^{true}}{\Lambda_c^{true}}$ again as a function of the invariant mass (bottom graphs (a) and (b)). For the top ones, the red curve shows the values assuming the perfect PID, the cyan one shows the values of the weighted Bayesian PID ($\Lambda_c^{measured}$) and the blue histogram shows the values of the Λ_c^{true}. The signal was amplified by a factor of one million and both the significance and the S/B ratio were accordingly rescaled.

3.3 Results

As already mentioned to apply the weighted Bayesian approach twenty steps of analysis were needed. After that, different graphs were prepared to compare the three approaches. For the analysis eight different momentum bins have been considered: 2-3,3-4,4-5,5-6,6-7,7-8,8-9 and 9-10 GeV/c.
Moreover all the results are shown as functions of the transverse momentum p_{T} of the Λ_c.

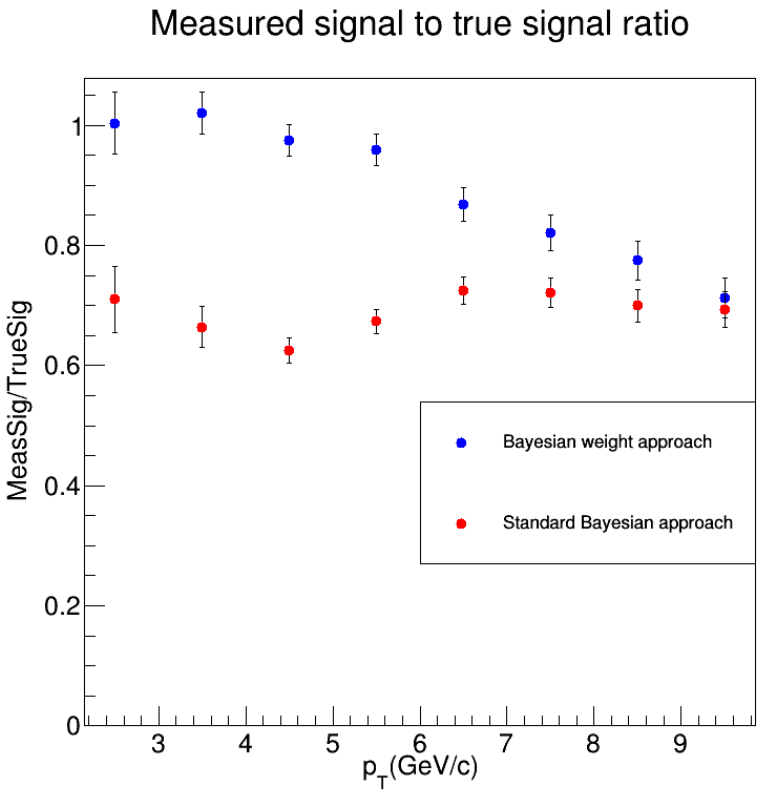

Figure 3.6: The plot shows the values of the ratio between the measured signal and the true signal (MeasSig/TrueSig) for different momentum bins. Blue dots refer to the weighted Bayesian approach, while the red ones refer to the standard Bayesian approach.

Fig. 3.6 shows that the efficiency of the weighted Bayesian approach used is higher compared to the standard Bayesian one. In fact, the mean value of MeasSig/TrueSig for the former is ≈ 0.9, while for the latter is ≈ 0.7. The efficiency values for the Nσ approach haven't been shown in this plot because they would have been close to 1 by definition.
Another key point of the study presented here is that the background signal must be reduced to the minimum. Fig. 3.7 shows the differences among the three used PID methods.
Data show how the use of the iterative approach allows to have the highest S/B values, resulting from a decrease of the background signal,combined with a slight increase of the

measured signal.
Consequently this leads to an increase of the signal significance[3], whose values are shown in Fig. 3.8.

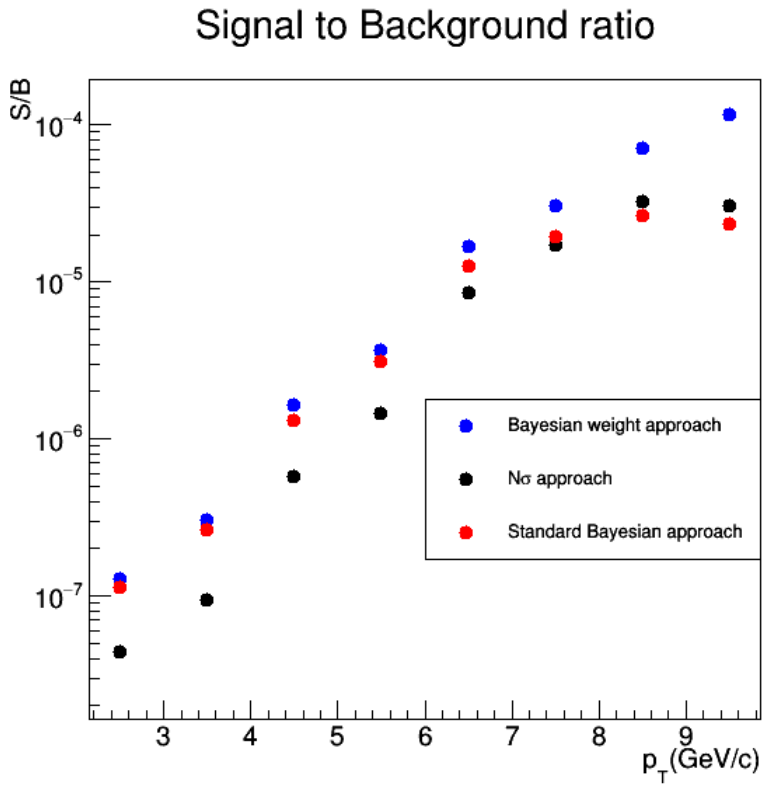

Figure 3.7: Signal/Background plot. Black dots are the values obtained using the cuts approach, while blue and red dots refer both to the Standard Bayesian and weighted Bayesian approaches as in Fig. 3.6. The vertical axis is in logarithmic scale.

The plot shows that, as expected, the significances are remarkably higher increasing the statistics. For example, the significance at RUN2 for the new approach in the 9-10 GeV/c bin is ≈ 2, while at RUN3 the significance reaches ≈ 40 in the same bin.
Data obtained are consistent with our hypotheses, as a matter of fact the significance for the new approach is always bigger than for the other two methods, whose significances are, instead, similar.
To further highlight the differences among the approaches significances, the histograms in Fig. 3.9 were realized using as momentum intervals the values [2-7] and [7-10] GeV/c, which are the ones where the Λ_c detection is more promising.
As before, Fig. 3.9 shows a clear increase of the significance for the weighted approach, which confirms the highest efficiency of the weighted Bayesian method for the Λ_c identification.

[3]Computed using Eq. 3.3

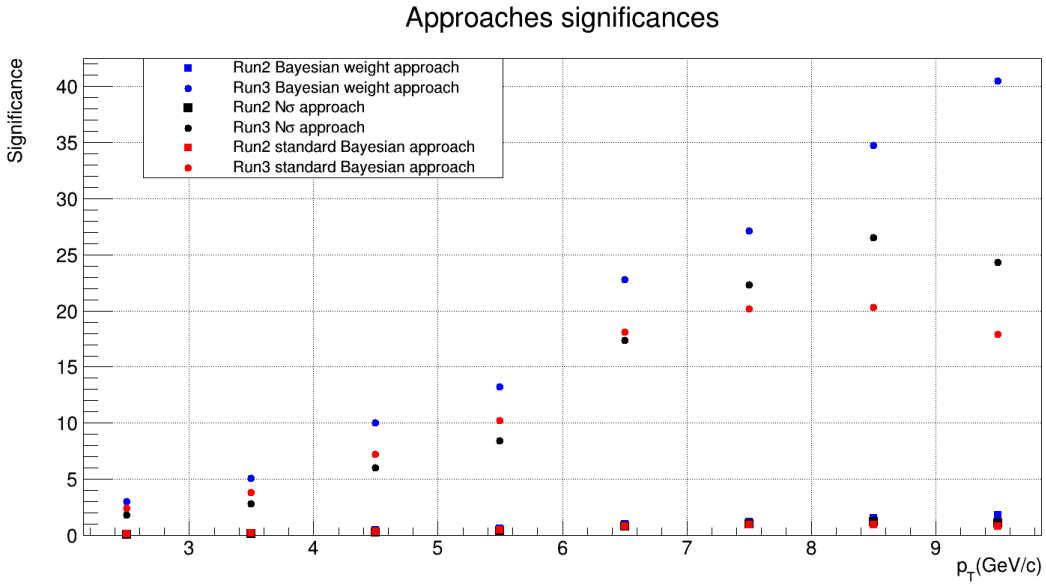

Figure 3.8: Significance of the signal for the three approaches as a function of the Λ_c transverse momentum p_{T}.

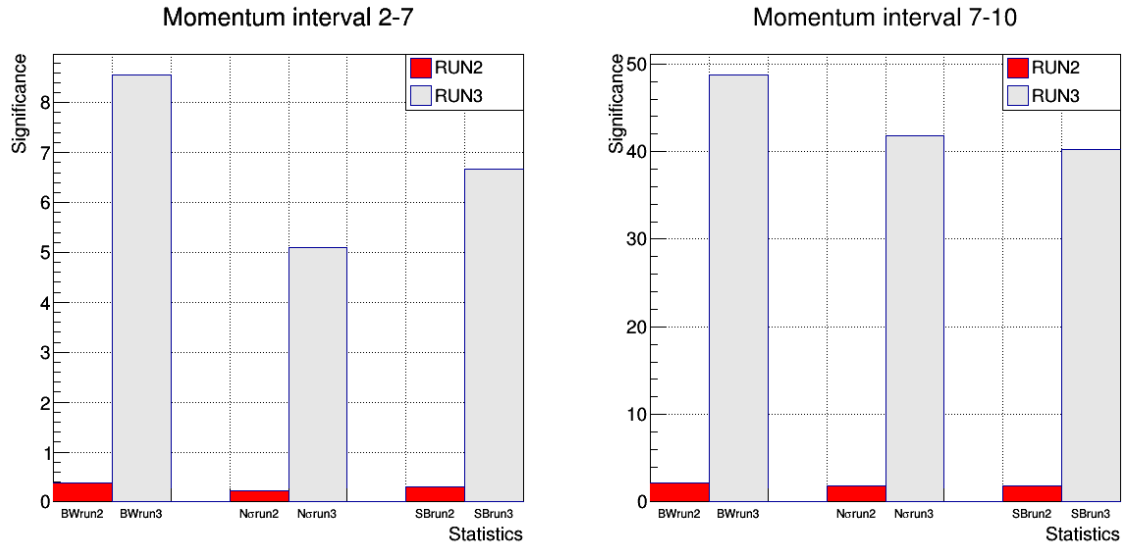

(a) (b)

Figure 3.9: Histograms of significance as a function of the statistics: (a) shows the data for the momentum interval 2-7 GeV/c; (b) shows the data for the momentum interval 7-10 GeV/c. Acronyms used: BW = Bayesian Weights; $N\sigma$ = number of σ for the cut; SB = Standard Bayesian.

Conclusions

In this thesis a feasibility study on the detection of the Λ_c baryon with the ALICE detector in PbPb collisions during RUN2 and RUN3 LHC data taking periods was presented. The study was focused on a new approach to perform particle identification (PID), replacing the usual cut–based method on the detector signals with a one using probabilities derived using the Bayes theorem (used as weight), namely "Weighted Bayesian".
The results obtained showed that the method is close to mimic a perfect PID scenario and superior to standard ALICE PID cut-based approaches, both in terms of significance and of the S/B ratio in the full momentum range under consideration.
In particular, the significance was evaluated assuming LHC RUN2 and RUN3 expected event statistics and the conclusion is that the Λ_c baryon will be accessible in a wide p_T range only at RUN3.
The new method, which is the natural evolution of the well tested "Bayesian PID as a cut", was investigated using a fast simulation. To better quantify the performance of the new method, a full simulation instead of a fast one could be performed in future to verify our results in a fully realistic scenario.

Bibliography

[1] N. Semprini Cesari (2015), Corso di laurea in Fisica, *Appunti di lezione di Fisica nucleare e subnucleare 2014/2015*, Università di Bologna

[2] Dr. Cristophe Clement, http://www.fysik.su.se/∼clement/teaching/emparfys/2010-2011/Lecture12.pdf Stockholm University (2011)

[3] http://www.nobelprize.org/nobel_prizes/physics/laureates/2004/popular.html

[4] A. Jaffe, E. Witten *"Millennium Prize Problem"*, http://www.claymath.org/library/monographs/MPPc.pdf

[5] Z. Fodor, S.D. Katz, *"The phase of quantum chromodynamics"* arXiv:0908.3341v1 (2009)

[6] Johann Rafelski and Jean Letessier, *Hadron Freeze-out and QGP Hadronization* arXiv:9902365v1 (1999)

[7] Dr. Francesca Bellini, Ph.D. Thesis *Measurement of* $K(892)^{*0}$ *resonance production in Pb–Pb collisions with the ALICE experiment at the LHC* (2013)

[8] A. Festanti, Thesis: *Calibrazione dell'effetto di "time walk" per il rivelatore TOF dell'esperimento ALICE* (2009)

[9] V. Koch *Introduction to Chiral Symmetry* (1995)

[10] J. Rafelski and R. Hagedorn, *From hadron gas to quark matter II* (1981)

[11] T. Matsui and H. Satz, *"*J/ψ *suppression by quark-gluon plasma formation"*, Phys. Lett. B178 (1986)

[12] P. Shukla, *"*J/ψ *suppression and enhancement at LHC"*, Proceedings of the International Symposium on Nuclear Physics (2009) (2009)

[13] E. Bratkovskaya, *"Phenomenology of photon and di-lepton production in relativistic nuclear collisions"*, arXiv:1408.3674 (2014)

[14] G. García Martínez, *"Advances in Quark Gluon Plasma"*, arXiv:1304.1452v1 (2013)

[15] ALICE Collaboration, Int. J. Mod. Phys. A 29 (2014) 1430044 *"Performance of the ALICE Experiment at the CERN LHC"*,

[16] A. Andronic , P. Braun-Munzinger, K. Redlich , J. Stachel, *"The statistical model in Pb-Pb collisions at the LHC"*, arXiv:1210.7724v1 (2012)

[17] CMS collaboration, *"Observation and studies of jet quenching in PbPb collisions at* $\sqrt{s_{NN}} = 2.76$ *TeV"*, arXiv:1102.1957v2 (2011)

[18] ALICE collaboration, *"Centrality determination of Pb–Pb collisions at* $\sqrt{sNN} = 2.76$ *TeV with ALICE"*, arXiv:1301.4361v3

[19] A.V.Khanzadeev, V.N.Nikulin, V.V.Poliakov, V.M.Samsonov,

[20] Y. Pachmayer, *"Physics with the ALICE Transition Radiation Detector"*, arXiv:1112.2098v1 (2011)

[21] C. Zampolli, *"Particle Identification with the ALICE detector at the LHC"*, arXiv:1209.5637v1 (2012)

[22] *"Particle identification in ALICE: a Bayesian approach"*, arXiv:1602.01392 (2016)

[23] C. Zampolli (2006), Ph.D. Thesis: *"A study of hadron yields and spectra with the ALICE experiment at LHC"*,

[24] M. Miller, K.Reygers, S.J. Sanders and P. Steinberg (2007), *"Glauber Modeling in High Energy Nuclear Collisions"*, arXiv:nucl-ex/0701025v1

[25] B. Abelev and ALICE Collaboration, *"*K^0_S *and* Λ *Production in Pb-Pb Collisions at* $\sqrt{s_{NN}} = 2.76$ *TeV"*, Phys. Rev. Lett. 111 (2013) 222301

[26] K. A. Olive *et al.* [Particle Data Group Collaboration], *"Review of Particle Physics"* Chin. Phys. C **38** (2014) 090001 and 2015 update.

[27] ZEUS collaboration *"Measurement of* D^+ *and* λ_c^+ *production in deep inelastic scattering at HERA"*, arXiv:1007.1945v2 (2010)

[28] T. Song, H. Berrehrah, D. Cabrera, W. Cassing, E. Bratkovskaya, *"Charm production in Pb+Pb collisions at the Large Hadron Collider Energy"*, Phys. Rev. C 93, 034906 (2016) arXiv:1512.00891

[29] The ALICE collaboration, *"Measurement of charm production at central rapidity in proton–proton collisions at* $\sqrt{s}$*=2.76 TeV"*, arXiv:1205.4007v2 (2012)

[30] Y. Oh, C. M. Ko, S. H. Lee and S. Yasui, *"Heavy baryon/meson ratios in relativistic heavy ion collisions"*, arXiv:0901.1382v1 (2009)

[31] D. d'Enterria, *"Hard scattering cross sections at LHC in the Glauber approach: from pp to pA and AA collisions"*, arXiv:nucl-ex/0302016

[32] ALICE Collaboration *"Centrality dependence of the charged-particle multiplicity density at mid-rapidity in Pb–Pb collisions at* $\sqrt{s_{NN}}$ *= 5.02 TeV"*, Phys. Rev. Lett. 116, 222302 (2016)